Experimental and Theoretical Investigation of Mesoporous MnO_2 Nanosheets with Oxygen Vacancy for High-Efficiency Catalytic $DeNO_x$

Jia Liu,[†,¶] Yajuan Wei,[†,‡,¶] Pei-Zhou Li,[†,¶] Peipei Zhang,[‡] Wei Su,[‡] Yan Sun,[‡] Ruqiang Zou,[§*] Yanli Zhao[†*]

[†]*Division of Chemistry and Biological Chemistry, School of Physical and Mathematical Sciences, Nanyang Technological University, 21 Nanyang Link, Singapore 637371.*
[‡]*High Pressure Adsorption Laboratory, Department of Chemistry, School of Science, Tianjin University, Tianjin 300072, PR China.*
[§]*Beijing Key Lab of Theory and Technology for Advanced Battery Materials, Department of Materials Science and Engineering, College of Engineering, Peking University, Beijing 100871, China.*

Abstract

Solvent-free synthetic method was employed for the construction of mesoporous α-MnO_2 nanosheets. Benefited from solid interface reaction, the obtained MnO_2 nanosheets with large oxygen vacancy exhibit high surface area of up to 339 m^2/g and mesopore size of 4 nm. The MnO_2 nanosheets as a catalyst were applied in NH_3-assited selective catalytic reduction (NH_3-SCR) of $DeNO_x$ at relatively low temperature range. The conversion efficiency could reach 100% under gas hourly space velocity (GHSV) of 700,000 h^{-1} at 100 °C. To gain insight into the mechanism about NH_3-SCR of nitric oxide on the MnO_2 nanosheets, temperature-programmed desorption of NH_3, density function theory study and *in situ* diffuse reflectance infrared Fourier transform spectra were carried out, revealing the cooperative effect of catalytic sites on the reduction of nitric oxide. This work provides a strategy for facile preparation of porous catalysts in low-temperature $DeNO_x$.

KEYWORDS: $DeNO_x$, Density function theory, Diffuse reflectance infrared Fourier transform, Mesoporous MnO_2, Selective catalytic reduction

Introduction

Excessive exhaust of NO_x produced by the combustion of fossil fuels has led to serious environmental issues such as chemical smog and acid rain. Selective catalytic reduction (SCR) as one of the most efficient $DeNO_x$ techniques has been widely employed in industry. However, a main drawback of commercial SCR technique is that it inevitably requires high operation temperature and involves with harmful components of flue gas to deeply impact the catalyst performance. Combing SCR equipment with the desulfurization system is an alternative method with advantages of avoiding poisoning effect of fly ash and SO_2 to catalysts. Meanwhile, relatively low temperature (such as 100 °C) of flue gas could prevent the porous structure of catalysts from destroying by water vapor. In order to develop low temperature SCR technique, catalysts owing high activity of SCR or NH_3-SCR are urgently demanded and widely explored, in which Mn-based catalysts have been considered one of the most promising candidates for their low temperature NH_3-SCR of NO.[1,2] Several Mn-based catalysts with amorphous state[3-6] and different shape in micro scale [7-10] prepared through various synthetic methods[11-15] and precursors[16-20] and coupled with a carriers[21-23] have been reported. In contrast to the $DeNO_x$ *via* commercial SCR catalysts[24,25] at high temperature, the NO reduction at low temperature should follow special routes. Some plausible routes have been proposed and proven by using isotopic labeled and *in situ* FT-IR studies. For instance, the SCR mechanism over the surface of titania-supported manganese catalysts showed that the products of the SCR reactions are mainly related to a coupling interaction between one nitrogen atom from ammonia and other one from nitric oxide. It was reported that water is not formed directly with the gas phase oxygen, but with the surface oxygen on the catalyst.[26] Some key steps of NH_3-SCR on Mn-based catalysts at low temperature have been proposed, including the NH_2 formation,[27-31] reduction of NO and dissociation of N_2O,[31,32] which determine the selectivity of SCR reaction. Evidently, all above aspects are related to the surface chemical property. In addition, the SCR reaction kinetics is also controlled by the diffusion, especially on highly porous catalysts.[33] It is reasonably considered that water diffusion is the most difficult one among all of reactants and products, and therefore competitive adsorption of water to NH_3 and NO on active sites would greatly lead to the reduction of SCR reaction rates. Currently, Mn-based SCR catalysts can be mainly classified into pure manganese oxide,[12,12,34] and their composites with metal oxides,[15,18,20,35-38] molecular sieves,[39] Al_2O_3,[40] activated carbon,[41] porous SiO_2,[40] carbon nanotubes,[42,43] and graphene.[44] General synthetic methods include hydrothermal reactions for manganese oxides, as well as co-precipitation and wet impregnation for complex catalysts. Due to coordinative effect of water molecule in these methods, Mn ions can migrate easily, resulting in the formation of large MnO_2 crystals with surface defect, non-porous structure, and low surface area.

To avoid the migration of surface atoms, herein, we report the one step strategy named as solid interface reaction (SIR) to synthesize mesoporous α-MnO_2 nanosheets. In contrast to the solvent method, reactants in SIR are not surrounded by solvent molecules such as water, meaning that the migration of atoms and groups are limited during the reaction process. Therefore, the self-assembly of formed surface is restricted, which efficiently prevents the formation of large crystals. In addition, defects formed on the surface can also be well

preserved without self-repairing. The obtained catalyst exhibits highly efficient performance for the $DeNO_x$ in NH_3-SCR at a relatively low temperature range. The impact of synthesis conditions on the surface property and structure of the catalyst was elucidated. Based on experimental results, reasonable reaction route and cooperative effect of Lewis-Brønsted acids were predicted by using density function theory (DFT) calculations and proven by *in situ* diffuse reflectance infrared Fourier transform (DRIFT) spectra.

Experimental section

Experiments. The MnO_x catalyst was synthesized by the SIR method, named as Mn-S. In a general procedure, $KMnO_4$ (0.08 g, 40-80 mesh) was mixed with three manganese(II) salts (CH_3COOH^-, Cl^- and NO^{3-}) (40-80 mesh). The molar ratio of $KMnO_4$ to Mn^{2+} was varied from 1.6 to 2.4. The mixed solid powder was fully grounded for about 5 min in an agate mortar to make them completely converted. The obtained materials were washed by alcohol (99.6%) to remove residual soluble salt. The product was separated from turbid liquid by centrifugation. The sample was finally dried at about 180 °C under vacuum for 6 h, while the calcination at high temperature (over 500 °C) may decompose the material. The MnO_x catalyst was also synthesized by the precipitation method as a control, named as Mn-P-Ac. Basically, $KMnO_4$ (0.08 g) and $MnAC_2$ (0.2 g) were dissolved in deionized water (10 mL and 5 mL) at room temperature, respectively. The solutions were quickly mixed with rigid stirring for 1 min. The obtained sediment was centrifugally separated and washed by deionized water for several times for the removal of soluble ions. The sample was dried at 180 °C under vacuum for 6 h.

The setup for the measurement of NH_3-SCR catalytic activity was assembled by us as shown in Scheme S1 (Supporting Information). The catalyst (100 mg) was compacted in a stainless-steel reactor (internal diameter = 4 mm) for each test. The contents of NO, NO_x (converted to NO by the catalyst), N_2O and NH_3 were measured by an FTIR spectrometer Model QGS-08C purchased from Beijing BAIF-Maihak Analytical Instrument Co. Ltd. Flow rate was controlled by mass flow controllers. During the experiments, the feed gases were mixed in reactor. By controlling the flow rate of three feed gases, the mixed gas passing through the reactor consists of NO (0.04 %), NH_3 (0.04 %), and O_2 (4 %) balanced by N_2. The tests were conducted at a temperature range from 30 °C to 260 °C under a flow rate of 180 mL/min. The tests were also conducted under a GHSV range from 100,000 h^{-1} to 700,000 h^{-1} at 100 °C. Stability tests for Mn-S-Ac-1.5 were conducted at 120 °C under GHSV of 50,000 h^{-1} with conditions of NO (0.04 %), NH_3 (0.04 %), O_2 (4 %), and H_2O (5%) balanced with N_2. Each test was processed about 90 min for obtaining stable NO conversion. The N_2 selectivity (S_{N2}) an NO conversion (η_{NO}) were calculated by the following equations:

$$\eta_{NO} = \frac{C_{NO,in} - C_{NO,out}}{C_{NO,in}} \times 100\% \quad (1)$$

$$S_{N2} = \frac{(C_{NO,in} + C_{NH3,in}) - (C_{NO,out} + C_{NH3,out}) - 2C_{N2O,out} - C_{NO2,out}}{(C_{NO,in} + C_{NH3,in}) - (C_{NO,out} + C_{NH3,out})} \times 100\% \quad (2)$$

where $C_{NO,in}$/$C_{NH3,in}$, $C_{NO,out}$/$C_{NH3,out}$, C_{NO2} and C_{N2O} stand for input and output amounts of NO, NH_3, NO_2 and N_2O, respectively.

Calculations. The details about the DFT calculations involving the Perdew–Burke–Ernzerhof (PBE)[45] functional and projector augmented wave method (PAW)[46,47] are shown in the Supporting Information.

Results and discussion

Three manganese salts including $Mn(Ac)_2$•$4H_2O$, $Mn(NO_3)_2$•$4H_2O$ and $MnCl_2$•$4H_2O$ and three molar ratios of Mn^{2+}/MnO_4^- (1.2, 1.5, and 1.8) were selected in order to investigate the impact of counter ions and molar ration of two reactants on final structure of the product. The obtained samples named as Mn-S-M-n (M: Ac, NO_3 and Cl; n = 1.2, 1.5, 1.8 corresponding to the molar ratio of Mn^{2+}/MnO_4^-). The porous structure information of the obtained samples under different synthesis conditions calculated from N_2 isotherm curves (Figures S1-S3) at 77 K is listed in Table 1.

Typical SIR process when using $Mn(Ac)_2$ and $KMnO_4$ as reactant is shown in Figure 1a. The color changes of the solid mixture from purple to dark brown indicate that the reaction occurred. With continuously grinding, more surfaces of both reactants were exposed to interact for complete conversion. In contrast, the mixture without grinding cannot be converted to MnO_2 completely, which was proven by comparing powder X-ray diffraction (XRD) patterns as shown in Figure S4. The obtained product by SIR showed a layered structure as shown in Figure 1a. We applied time-resolved *in situ* Raman spectroscopy to study initial stages of SIR between $KMnO_4$ and $Mn(Ac)_2$. The estimated 1.3 μm laser spot was focused on the interface of crystals of $KMnO_4$ and $Mn(Ac)_2$. The time-resolved *in situ* Raman spectra were collected as shown in Figure 1b. The laser (8 mW, 532 nm) was used not only as the light source, but also could drive the SIR reaction in place of grinding. During continuous irradiation by the laser, evident changes of spectra were observed. The band at 838 cm^{-1} assigned to symmetric vibration of MnO_4^- almost disappeared after a long-time irradiation, accompanied with a band increase at 650 cm^{-1}. At the same time, the band at 166 cm^{-1} decreased due to symmetric vibration of Mn(II)-H_2O. These changes indicate that the reaction between $KMnO_4$ and $Mn(Ac)_2$ occurred at the interface. It was worth noting that the Raman spectra (Figure 1b) also showed the scattering peaks of $KMnO_4$ and $Mn(Ac)_2$. The possible explanation is that the laser spot lighted on the interface covers not only the interface area, but also part of unreacted $KMnO_4$ and $Mn(Ac)_2$. Comparing with pure MnO_2 sample, the band at 1450-1500 cm^{-1} corresponding to aromatic

ring (C-C) vibration and the band at 950 cm^{-1} corresponding O-C-O vibration were always present during the whole irradiation period, indicating that the reactants outside the interface cannot be converted to MnO_2 without grinding. Thus, the results demonstrated that the reaction occurred at the interface.

It is interesting that, after washed by alcohol, the obtained solid can disperse in alcohol or water by ultrasonic oscillation and turn into deep yellow solution. As shown in Figure 1c, the solution presents obvious absorption of ultraviolet light at 374 nm, which is a characteristic peak of thick layered MnO_2 nanosheet attributed to the *d-d* transition of Mn^{4+} ions in the MnO_6 octahedra of MnO_2 nanosheet.[48,49] The average thickness of the nanosheets was 3 nm measured by atomic force microscopy (AFM) as shown in Figure 1d. The Mn-S-Ac-1.5 sample synthesized from $Mn(Ac)_2$ and $KMnO_4$ with the molar ratio of 1.5 (Mn^{2+}/MnO_4^-) *via* the SIR method shows type IV isotherm curve (Figure 1e) defined by IUPAC, indicating a mesoporous structure. It also possesses ultrahigh surface area about 339 m^2/g and mesopore size about 4 nm (Figure 1e insert). In order to make the comparison, the N_2 isotherm curve of MnO_2 synthesized from $Mn(Ac)_2$ by the solution precipitation method was collected at 77 K (Figure S5). The obtained sample shows larger pore size than those obtained from same manganese salts *via* the SIR method. It is remarkable that the surface area of the Mn-P-Ac sample is over 400 m^2/g. Thus, the Mn-S-AC-1.5 and Mn-P-Ac samples owing larger surface areas were selected as candidates for NH_3-SCR of NO.

Scanning electron microscopy (SEM) and transmission electron microscopy (TEM) images were then collected. The sample Mn-S-Ac-1.5 presented a layered structure as shown in Figure S6a. In contrast, Mn-P-Ac presented amorphous nanoparticles (Figure S6b). Evidently, the Mn-S-Ac-1.5 sample possesses a nanosheet structure as shown from TEM images of Figure 2a,b. The nanosheet structure of MnO_2 is attributed to the unique SIR method, which can only occur on the interface of $KMnO_4$ and $Mn(Ac)_2$. After peeling from the interface, the reaction continues to carry out on freshly exposed surface. The peeled MnO_2 nanosheet could assemble more or less to form a layered structure and generate slit pores. The distance between each layer was determined by the layer thickness (3-4 nm). High-resolution TEM (HRTEM) images present irregular ovals (10× 20 nm) within the nanosheets. When further increasing the resolution, meshes (001) and (210) of α-MnO_2 were observed as shown in Figure 2b. Energy dispersive X-ray spectroscopy (EDS) reveals that the main elements of Mn-S-Ac-1.5 are Mn and O (Figure S7).

Table 1 Porous structure information of samples. PSD: pore size distribution.

Sample	Mn^{2+}/MnO_4^-	S_{BET} / m^2g^{-1}	Pore volume / cm^3g^{-1}	PSD / nm
Mn-S-Ac-1.2	1.2	233	0.272	5-7
Mn-S-Ac-1.5	1.5	339	0.287	3-5
Mn-S-Ac-1.8	1.8	160	0.348	6-15
Mn-S-Cl-1.2	1.5	156	0.224	4-6
Mn-S-Cl-1.5	1.2	334	0.327	4-6
Mn-S-Cl-1.8	1.8	211	0.298	4-6
Mn-S-NO_3-1.2	1.2	111	0.146	-
Mn-S-NO_3-1.5	1.5	48	0.055	-
Mn-S-NO_3-1.8	1.8	42	0.043	-
Mn-P-Ac-1.5	1.5	402	0.618	>18nm

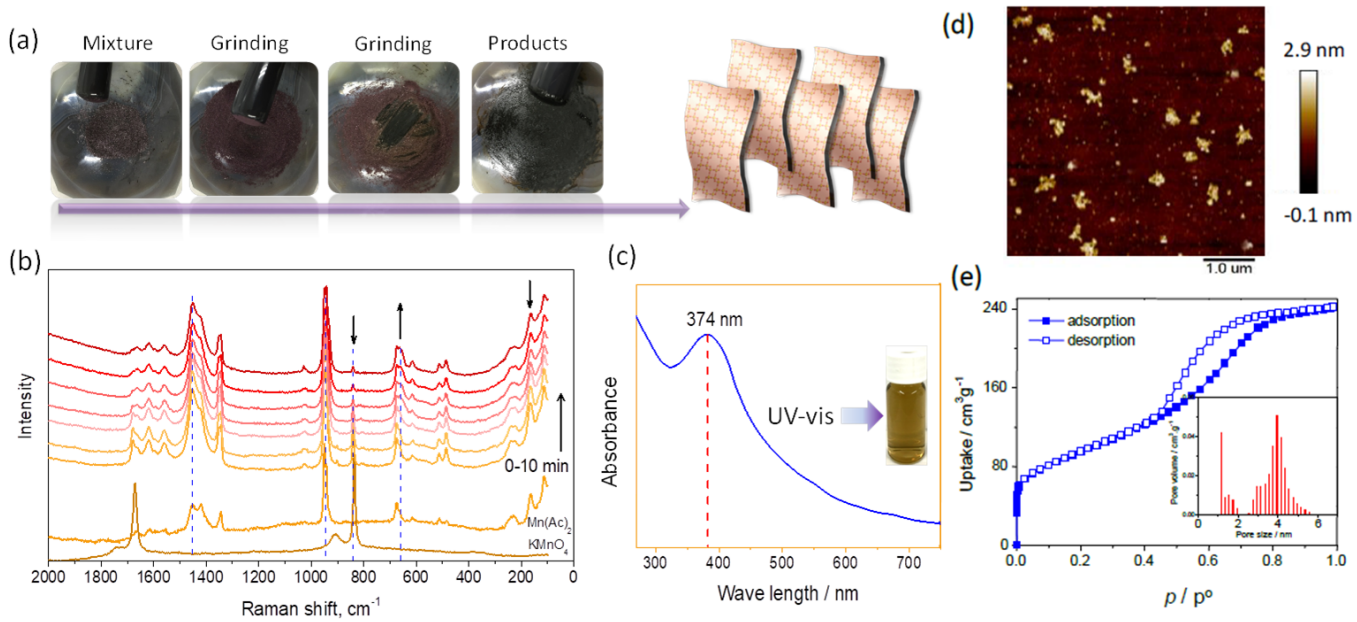

Figure 1. Preparation and characterization of a mesoporous α-MnO_2 nanosheet from SIR. (a) Color change of the mixture during SIR process, and schematic representation of mesoporous MnO_2 nanosheet. (b) Time resolved *in situ* Raman spectra of the interface between $KMnO_4$ and $Mn(Ac)_2$ as compared with Raman shifts of $KMnO_4$ and $Mn(Ac)_2$ along. (c) UV-vis spectrum of the Mn-S-Ac-1.5 sample dispersed in

deionized water. (d) AFM image of MnO_2 nanosheets. (e) N_2 isotherm curves of Mn-S-Ac-1.5 at 77 K and its DFT pore size distribution (insert).

To further confirm the structure of Mn-S-Ac-1.5, the synthesized materials were characterized by powder XRD. None of obvious diffraction peaks was identified from the Powder XRD pattern because of its nanosheet structure (Figure 2c). Similar observation was found on the Mn-P-Ac sample (Figure S8). The only identified peak around 37° may correspond to mesh (211) of α-MnO_2 or mesh (101) of β-MnO_2. To further analyze the crystal type, Raman spectra were conducted at room temperature because different crystal types could produce different Raman scattering signals due to their different vibration models. The α-MnO_2 materials could crystallize into a body centered tetragonal structure with a space group of I4/m. The factor group analysis shows that spectroscopic species of 6Ag + 6Bg + 3Eg are Raman-active.[50,51] The α-MnO_2 materials were reported to have two diagnostic Raman scattering bands at 574 and 634 cm^{-1}, corresponding to the Ag spectroscopic species originated from breathing vibrations of MnO_6 octahedra within a tetragonal hollandite-type framework.[51,52] As shown in Figure 2d, the Raman scattering spectrum of Mn-S-Ac-1.5 shows several contributions at 351, 573 and 638 cm^{-1}. Compared with Raman scattering spectrum of α-MnO_2 type materials at 634 cm^{-1}, about 4 cm^{-1} shift was observed, which should be resulted from the quantum confinement effect. In a nanoscale, the bandgap of MnO_2 nanosheet increases due to the splitting of energy level near Fermi energy level, which further enhances blue shift of Raman spectrum. Meanwhile, the spectrum at 577 cm^{-1} disappeared on account of limited layers in the nanosheet structure. Hence, it is evident that the MnO_2 nanosheet that presents a similar Raman scattering spectrum with a blue shift belongs to MnO_2 type materials.

X-ray photoelectron spectroscopy (XPS) was then conducted for elucidating the surface chemical property. For Mn 2p peaks as shown in Figure S9, two main peaks in the range from 640 eV to 660 eV (Figure 2e) could be observed for Mn $2p^{3/2}$ and Mn $2p^{1/2}$. By performing a peak-fitting deconvolution, the Mn 2p3/2 spectrum in Figure 2e was separated into peak I (641.9 eV) and peak II (642.9 eV).[53] Peak I is attributed to the Mn^{4+} binding energy form the surface of the nanosheet. On account of lacking the saturated binding with oxygen atom, the energy level of occupied *p* orbital from Mn^{4+} is higher, leading to relatively low electron binding energy of Mn $2p^{3/2}$. Compared with surface Mn^{4+}, the inner Mn^{4+} fully binds with oxygen atom. Therefore, more electrons from Mn *d* orbital transfer to oxygen, leading to a reduction of electron shield effect and higher core energy. Consequently, the enhancement of electron exciting energy results in higher binding energy level of electrons from Mn *p* orbital. The O1s peak was fitted into two portions (Figure 2f). The peak at 529.7 eV belongs to the lattice oxygen in MnO_2, and the surface adsorbed oxygen is attributed to the peak of 530.7 eV.

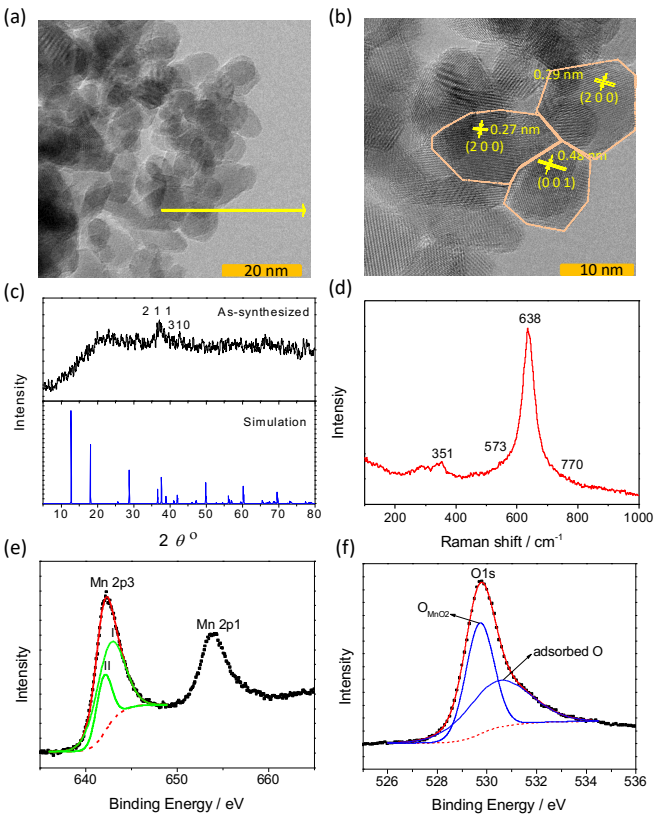

Figure 2. Structural characterization of Mn-S-Ac-1.5 nanosheet. (a,b) TEM images, (c) powder XRD pattern, (d) Raman spectrum at room temperature, (e) Mn XPS pattern, and (f) O XPS pattern.

It is obvious that adsorbed oxygen takes a large ratio probably due to a large amount of surface oxygen defect, which is beneficial to the oxygen process during the SCR reaction and enhanced N_2 selectivity.[54] When comparing between Mn-S-Ac-1.5 obtained by the SIR method and Mn-P-Ac from the precipitation method, it was found that Mn-S-Ac-1.5 exhibits wider temperature window from 80 °C to 200 °C with the NO conversion of 100% (Figure 3a). Even at 80 °C, the NO conversion by Mn-S-Ac-1.5 could almost approach 100%, which is not only in virtue of its high surface, but also attributed to the nanosheet structure. Both samples could keep high NO conversion below 200 °C. When further increasing the temperature above 200 °C, the NO conversion dropped quickly.

The NO conversion under a series of GHSV as shown in Figure 3b clearly presents different catalytic performance between the two samples. Apparently, the NO conversion of the Mn-S-Ac-1.5 sample synthesized from the SIR method could keep at a relatively high level under a large GHSV range from 100,000 h^{-1} to 700,000 h^{-1}. While the NO conversion on the Mn-P-Ac sample *via* the precipitation method dropped off sharply upon raising the GHSV. Several reasons could breed this different catalytic performance. First, more surface defects

of the Mn-S-Ac-1.5 sample may lead to fast O_2 adsorption for the NO oxidation and N_2O adsorption for the dissociation. Second, the LUMO orbital energy level of exposed Mn atom on Mn-S-Ac-1.5 is lower, further proving high binding energy of Mn 2p electrons observed in the XPS study, which promotes the NH_3 adsorption and NH_2 generation. Third, mesoporous structure of Mn-S-Ac-1.5 is beneficial to both the reaction collision and diffusion.[33] The water molecule diffusion related to the recovery of catalytic sites also plays an important role during the SCR of NO. Accordingly, Mn-S-Ac-1.5 had lower surface area than Mn-P-Ac, but better performance on account of its mesoporous structure.

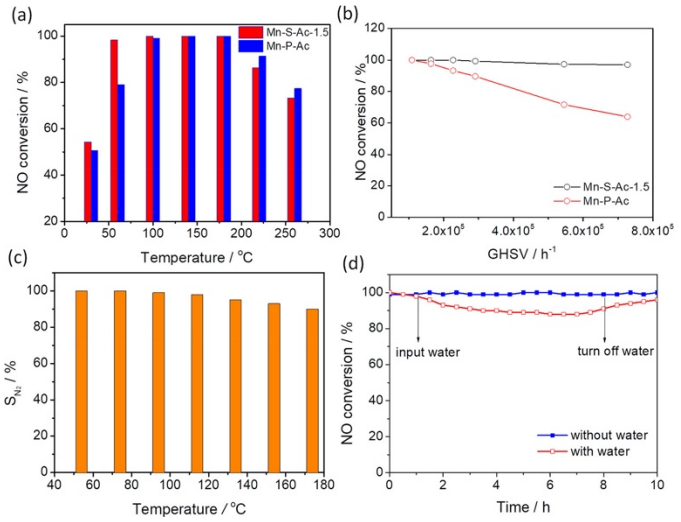

Figure 3. NH_3-SCR DeNO$_x$ performance. (a) NO conversion at the temperature range from 30 °C to 260 °C under a flow rate of 180 mL/min corresponding to the GHSV from 100,000 h^{-1}. (b) NO conversion at 100 °C under GHSV from 100,000 h^{-1} to 700,000 h^{-1}. (c) N_2 selectivity of Mn-S-Ac-1.5. (d) Stability tests of Mn-S-Ac-1.5 at 120 °C under GHSV of 50,000 h^{-1} with or without water. Conditions: NO (0.04 %), NH_3 (0.04 %), O_2 (4 %), and H_2O (5%) balanced with N_2.

The N_2 selectivity was calculated by detecting the N_2O concentration from outlet gas as presented in Figure 3c. The N_2 selectivity on Mn-S-Ac-1.5 decreased very slowly from 100% to about 90% when the temperature increased from 40 °C to 180 °C. High N_2 selectivity is mainly attributed to cooperative catalytic effect of Mn atoms and a large quantity of surface oxygen beneficial to the N_2O adsorption and dissociation.

The stability results of the Mn-S-Ac-1.5 catalyst are shown Figure 3d. After long time (10 hours) experiments without water, the NO conversion could still keep at high level, demonstrating a good stability of the catalyst. Since the exhaust flue gas contains a certain amount of water vapor (about 5%-8%), the effect of the water vapor on the NO conversion by the Mn-S-Ac-1.5 catalyst was investigated during the SCR process with GHSV of 50,000 h^{-1} at 120 °C. The results show that the presence of the water vapor led to a slight decrease of the NO conversion by the Mn-S-Ac-1.5 catalyst (Figure 3d). The NO conversion was decreased from 100 % to ca. 90 % after the addition of H_2O and remained at this level over 10 h. After removing water, the NO conversion was recovered above 95%, indicating that the water inhibition is basically reversible. The high resistance of this catalyst to H_2O is mainly due to its favorable stability, suitable porous structure, and large surface area. In low temperature SCR technology, the SCR setup contains the desulphurization system that can avoid catalysts to be exposed in SO_2 atmosphere.

NH_3-TPD curves of Mn-S-Ac-1.5 present two desorption peaks (Figure S10), indicating the existence of at least two types of acid sites.[55] NH_3 species binding with Brønsted acid sites and Lewis acid sites have been well studies through the FTIR analysis.[54-59] Brønsted acid sites corresponding to the peak around 270 °C are formed by oxygen atoms connected to Mn, where the negative charge generated is compensated by a proton. These sites are believed to be the catalytic center for NH_4^+ and H_2O formation. Lewis acid sites corresponding to the peak at 400 °C are composed of surface Mn atoms with unsaturated coordination, which are considered as catalytic centers for NH_3 adsorption, -NH_2 formation and NO conversion. Both peaks are wide and tailing, implying wide distribution of catalytic centers. Experimental result shows that the NO conversion reduces to about 70% above 200 °C, which is agreeable to the desorption temperature of NH_3 adsorbed on Brønsted acid sites. These observations reveal that the main part of SCR reaction occurs on Lewis sites, and the decrease of the NO conversion could be due to the absence of Brønsted acid catalytic effect.

The NH_3 adsorption and activation is the initial step of the whole SCR process. When NH_3 first adsorbs on Brønsted acid sites, NH_3 binds with H atom on the surface to form NH_4^+ group. After disassociated from the surface, NH_4^+ reacts with NO_2^- that generated from NO by α-MnO_2 to form NH_4NO_2 followed by the desorption of N_2 and H_2O. Experimentally, it was found that ammonia adsorption is much stronger on Lewis acid sites provided by unsaturated coordinative Mn atoms than on Brønsted acid sites from the surface hydroxyl group. We examined two possible adsorption sites based on the α-MnO_2 (001) model. The Lewis acid adsorption sites in our model are surface unsaturated coordinative Mn cations. Brønsted acid adsorption sites are from the surface hydroxyl groups. The optimized adsorption geometries are shown in Figure S11. The binding energy of NH_3 adsorbed on Lewis acid sites is about 0.7 eV higher than that on Brønsted acid, indicating that NH_3 prefers to adsorb on Lewis acid sites. Studies showed that the SCR presented high activity even at about 50 °C, and the reaction mechanism should follow the Langmuir-Hinshelwood (L-H) mechanism.

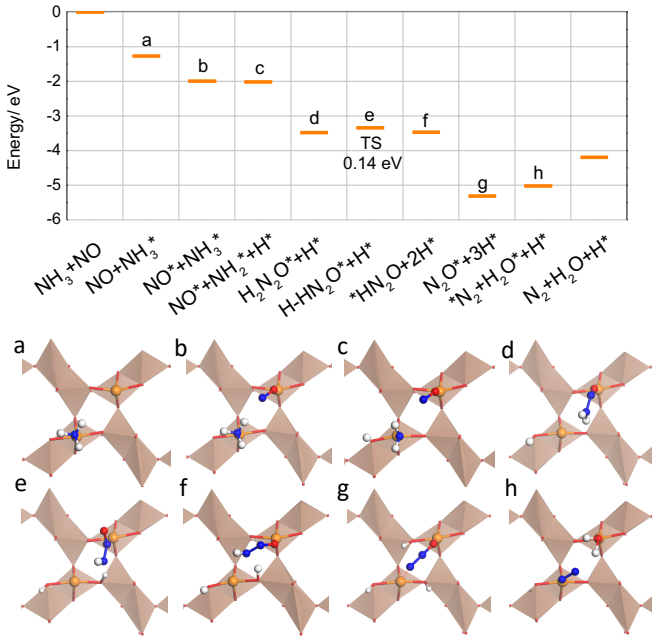

Figure 4. **DFT studies of reaction pathway for NO reduced by NH_3 on α-MnO_2 (001) system**. The calculated energy for the reaction is indicated on the upper side of the figure. The optimized structures of each state are included on the bottom side of the figure. Colors: O (red), H (white), N (blue), surface Mn (golden), and MnO_2 (polyhedron).

To provide a molecular description of the NO reduction on our system, we performed DFT calculations to search for possible intermediates and build a plausible reaction pathway. The binding NH_3 on α-MnO_2 (001) mesh was investigated by the DFT study. It was observed that the distance between Mn atom and N_{NH3} atom is about 2.16 Å (Figure 4a). Strong interaction between Mn and N_{NH3} was attributed to the electron density transferring from sp^3 orbital of NH_3 to dz^2 orbital of Mn atom. Under the effect of Lewis acid Mn, the bond length of N-H_{NH3} was elongated from original 1.02 to 1.03 Å. Consequently, combined with hydrogen bonding effect of nearby O atom, the dissociation of one of the N–H bonds is very facile without obvious energy barrier. The resulting state involving adsorbed NH_2 and surface OH group is shown in Figure 4b. The distance between N_{NH2} and Mn^{4+} is about 1.98 Å, which implies stronger interaction. The binding energy was about 1.26 eV. The spin number of Mn atom increased from 3.9 to 4.20 indicates the electron transfer from N atom to Mn atom. The *d* orbital of Mn^{4+} could offer empty positions for electrons from N_{NH2}, providing suitable conditions for the Mn^{4+} reduction.

The NO adsorption could also occur on fresh Mn^{4+} Lewis acid sites, but with a relatively weak interaction as compared with NH_3. The binding energy was calculated to be about 0.71 eV. The N-Mn distance is 2.264 Å and the N-O bond is elongated from 1.197 to 1.216 Å. It was worthy to note that, if the adsorption of NO and NH_3 occurs on Mn^{4+} located at 1 × 1 channel as show in Figure 4b, adsorptive molecules could react to produce the transition state intermediate with low state energy and energy barrier. After the NH_2NO formation, the spin number of Mn atom increases to 4.26, indicating that Mn^{4+} is reduced to Mn^{3+}. After transferring the electron from NH_2 to Mn^{4+}, the NH_2 group with an unpaired electron prefers to react with NO to form NH_2NO with large delocalized π electron bonds. When anti-bond of NO is occupied by one electron, the N-O distance increases to 1.251 Å, indicating that the bond of NO is weakened (Figure 4d). NH_2NO could be dissociated to N_2O during high temperature SCR reaction. At low temperature, the cooperative reaction occurs at step d (Figure 4d). One of H atoms from NH_2NO approaches to the bridging O atom to form hydroxyl group. After the dissociation of both H^+, the two electrons of N_2O^{2-} focused O atom would lead to full occupation of oxygen *p* orbital to form O^{2-} ion under catalytic effect of Mn^{4+}. Through cooperative effect by two unsaturated bonding of Mn atoms located at the diagonal of α-MnO_2 1 × 1 channel (Figure 4g), N_2O is dissociated to N_2 and O^{2-}. Consequently, H_2O is formed and dispersed to expose fresh Mn^{4+} for next cycles.

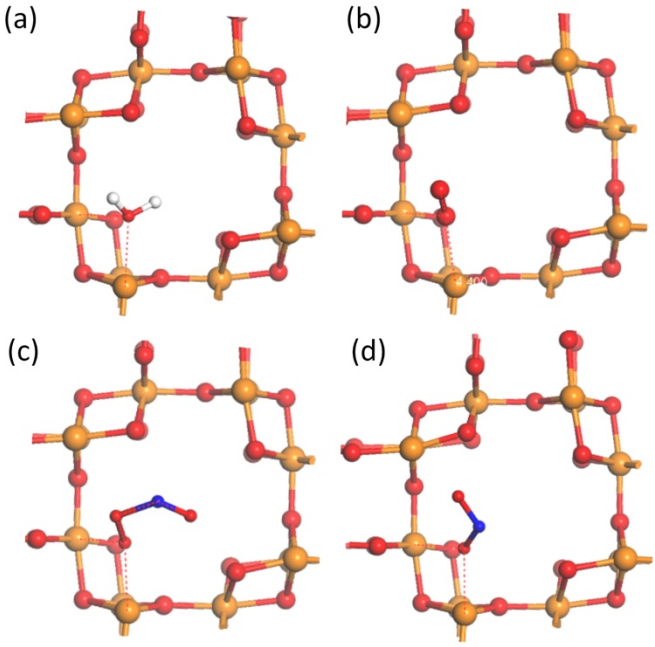

Figure 5. **Reaction mechanism.** (a) Formation of oxygen vacancy on the α-MnO_2 (001) system. (b,c) recovery of O vacancy on the α-MnO_2 (001) system by O_2, and (d) recovery of O vacancy on the α-MnO_2 (001) system by NO_2 during the NH_3-SCR process. Colors: O (red), H (white), N (blue), and surface Mn (golden).

Back to step c (Figure 4c), after the NH_2 desorption from the Mn^{4+} atom, Mn^{4+} is reduced to Mn^{3+}. After another process of NH_3 adsorption and dissociation, Mn^{3+} is further reduced to Mn^{2+}. The *d* orbital of Mn^{2+} is filled by 5 electrons, resulting in stronger shield effect on the atom core than the *d* orbital of Mn^{4+}. The stronger shield effect directly weakens the Mn^{2+}-O^{2-} bond. Therefore, the bridging O atom connected with two Mn atoms is facilely converted to H_2O with

Brønsted acid H^+. The calculation results showed that the distance between Mn and O is elongated from 1.96 to 2.42 Å, indicating that Mn-O bond is broken, and H_2O is formed as shown in Figure 5a. After the H_2O desorption, detached bridging O invites the oxygen defect, which could accept the oxygen atom from O_2 and NO_2 for the oxidation of Mn^{2+} to Mn^{4+} and recovery of the bridging O. Thus, one of plausible pathways for Mn^{2+} oxidation and recovery of oxygen vacancy was proposed. When O_2 molecule approaches to the oxygen vacancy, partial electron of Mn^{2+} shifts to the O atom, resulting in the electron occupation in antibonding orbital π^* of O_2. Therefore, the O-O bond length is elongated to 1.32 Å (Figure 5b). Under cooperative effect of free NO molecule, the O-O bond is further weakened and facilely broken (Figure 5c). Finally, one of broken O atoms occupies the oxygen vacancy, and the other active O atom reacts with NO to form NO_2 that would participate in the Mn^{2+} oxidation. As compared with O_2, NO_2 adsorbed at the oxygen vacancy could easily decompose to form NO and bridging O connected with two Mn ions, which enhances the reaction rate. When involving NO_2 into the system, the O atom of NO_2 prefers to locate at the oxygen vacancy as shown in Figure 5d. The spin number of Mn^{2+} atom decreases from 4.6 to 4.0, indicating that electrons from *d* orbital of Mn^{2+} transfer to the antibonding orbital of N_2O. The O_{NO2}-Mn distance was calculated to be 2.1 Å, which approaches to the standard Mn-O distance in the α-MnO_2 crystal. The distance (1.38 Å) between N and O located at the oxygen vacancy is obviously longer than normal N-O bond of NO_2 (1.21 Å), indicating the dissociation of NO_2. Finally, the vacancy is occupied by the O atom dissociated from NO_2, and the reduced Mn^{2+} atom is oxidized to Mn^{4+} for next cycles.

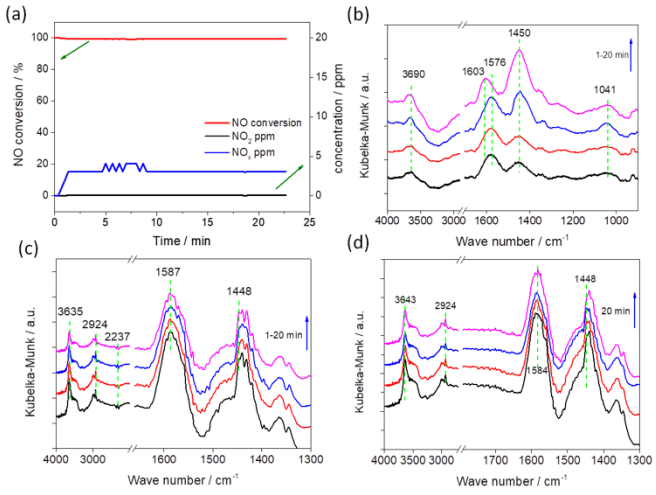

Figure 6. (a) SCR performance of Mn-S-Ac-1.5 at 120 °C under flow rate of 150 mL/min; (b-d) DRIFT spectra of Mn-S-Ac-1.5 at 120 °C with a total flow rate of 150 mL/min exposed to (b) 1000 ppm NH_3, (c) 1000 ppm NH_3 + 1000 ppm NO, and (d) 1000 ppm NH_3 + 1000 ppm NO + 3.2% O_2.

During the reaction, one electron from NH_3 transfers to the Mn^{4+} atom, and NH_2 reacts with NO to form N_2 and H_2O under catalytic activation and cooperative effect on the Mn-O-Mn unit. For further reduction of Mn, the oxygen vacancy appears which is repaired by O atom from NO_2 and O_2. Meanwhile, the reduced Mn^{2+} is oxidized to Mn^{4+} for the reuse. DRIFT spectra (Figure 6) were obtained by using NICOLET iS50 FT-IR spectrometer with 4 cm^{-1} resolution and 64 scans. The background spectrum was recorded with the flowing of N_2 and subtracted from the sample spectrum. The total flow rate was 150 mL/min.

SCR catalytic performance of Mn-S-Ac-1.5 (Figure 6a) was further evaluated by DRIFT spectra in order to better understand the NH_3 adsorption on Lewis acid sites and decomposition. DRIFT spectra of the sample exposed in 1000 ppm NH_3 at 120 °C were collected as shown in Figure 6b. Several bands at 1576, 1450, 1268, 1041 cm^{-1} and 3690 cm^{-1} were detected. The bands at 1580 and 1268 cm^{-1} could be attributed to coordinated NH_3 on Lewis acid sites.[56,57] The band at 1450 cm^{-1} is assigned to NH_4^+ species on Brønsted acid sites which agrees with NH_3-TPD experiment results.[1,2] The bands around 3690 cm^{-1} enhanced upon increasing the exposing time could be assigned to the surface O-H stretching which come from the formed Brønsted acid due to the decomposion of adsorbed NH_3 on Lewis acid sites. The bands at 1041 cm^{-1} could be assigned to gas-phase NH_3. When introducing NO (1000 ppm) into the system, obvious changes of bands around 1440 cm^{-1} and 1580 cm^{-1} were detected as shown in Figure 6c. The bands at 2924 and 1580 cm^{-1} could be attributed to N-O and N-H vibrations of NH_2NO, which well indicate the formation of intermediate products calculated from our DFT studies.[33,54] The enhancement of bands around 1450 and 3635 cm^{-1} could be assigned to the new Brønsted acid sites formed from NH_2NO_2 decomposition and H transferring to oxygen. The small band at 2237 cm^{-1} could be assigned to N_2O adsorption on Lewis acid site Mn^{3+} that then dissociated into N_2 and H_2O.[53] Then the catalysts were treated with 1000 ppm NH_3 and 1000 ppm NO for 30 min, followed by purging with O_2 and corresponding spectra (Figure 6d) were recorded. It was obvious that the IR band intensity around 3640-3400 cm^{-1} assigned to N-H stretching vibration of NH_3 or NH_2 decreased. The band intensity at 1448 cm^{-1} and 1587 cm^{-1} should be assigned to NH_3 adsorbed on Lewis acid Mn^{4+} and NH_4^+ adsorbed on Brønsted acid site respectively, which were weakened after introducing oxygen. Therefore, it was concluded that the SCR reaction on Mn-S-Ac-1.5 takes place by following the route we proposed from the DFT study.

Conclusion

In this work, we have demonstrated a novel solvent-free SIR synthetic strategy for the preparation of MnO_2 nanosheet catalyst possessing high surface area and mesoporous structure. Comparing

with other reported low temperature catalysts for the NO reduction, a significant enhancement of low temperature NH_3-SCR activity has been achieved by using the MnO_2 nanosheet. The NO conversion could reach 100 % at a temperature of 100 ^oC under high GHSV of 700,000 h^{-1}. The activity for NO reduction at low temperate by the present catalyst is about four times higher than other reported catalysts so far (Table S1). The stability tests have revealed that the catalyst could remain high NO conversion even under humid conditions. The NH_3 TPD analysis has indicated that large Lewis acid sites play the main role for enhancing the SCR activity. The DFT study and *in situ* DRIFT has been employed to investigate the NH_3 adsorption and conversion process on exposed surface of MnO_2 nanosheet, revealing that fast NH_3 adsorption and conversion are due to lower orbital energy level of exposed Mn atom on MnO_2 nanosheet and cooperative effect of nearby catalytic sites. Having the advantages of large surface area, highly active catalytic centers, unique geometric structure and optimal pore size for diffusion, the MnO_2 nanosheet is very promising in overcoming present bottlenecks of short usage time and high energy cost of catalysts toward future industrial applications.

Supporting Information

Schematic representation of experimental setup, N_2 isotherm curves, SEM images, EDS spectrum, powder XRD patterns, XPS patterns, NH_3 TPD curve, and the comparison of catalytic activity.

Acknowledgments

This work was supported by the National Natural Science Foundation of China (No. 21406004 and 51772008), the Singapore Academic Research Fund (No. RG121/16, RG11/17, and RG114/17), and the Singapore Agency for Science, Technology and Research (A*STAR) AME IRG grant (No. A1783c0007).

Authors Information

Corresponding Author

Email: zhaoyanli@ntu.edu.sg; rzou@pku.edu.cn

¶These authors contributed equally to this work.

References

(1) Boningari, T.; Smirniotis, G. P. Impact of Nitrogen Oxides on the Environment and Human Health: Mn-Based Materials for the NO_x Abatement. *Curr. Opin. Chem. Eng.* **2016**, *13*, 133–141.

(2) Li, J.; Chang, H.; Ma, L.; Hao, J.; Yang, R. T. Low-Temperature Selective Catalytic Reduction of NO_x with NH_3 over Metal Oxide and Zeolite Catalysts—A Review. *Catal. Today* **2011**, *175*, 147-156.

(3) Patel, A.; Shukla, P.; Chen, J.; Rufford, T. E.; Rudolph, V.; Zhu, Z. Activity of Mesoporous-MnO_x (m-MnO_x) and CuO/m-MnO_x for Catalytic Reduction of NO with CO. *Catal. Today* **2013**, *212*, 38-44.

(4) Wang, X.; Zheng, Y.; Xu, Z.; Wang, X.; Chen, X. Amorphous MnO_2 Supported on Carbon Nanotubes as a Superior Catalyst for Low Temperature NO Reduction with NH_3. *RSC Adv.* **2013**, *3*, 11539-11542.

(5) Jiang, H.; Wang, C.; Wang, H.; Zhang, M. Synthesis of Highly Efficient MnO_x Catalyst for Low-Temperature NH_3-SCR Prepared from Mn-MOF-74 Template. *Mater. Lett.* **2016**, *168*, 17-19.

(6) Deng, S.; Zhuang, K.; Xu, B.; Ding, Y.; Yu, L.; Fan, Y. Promotional Effect of Iron Oxide on the Catalytic Properties of Fe-MnO_x/TiO_2 (Anatase) Catalysts for the SCR Reaction at Low Temperatures. *Catal. Sci. Technol.* **2016**, *6*, 1772-1778.

(7) Zhang, J.; Li, Y.; Wang, L.; Zhang, C.; He, H. Catalytic Oxidation of Formaldehyde over Manganese Oxides with Different Crystal Structures. *Catal. Sci. Technol.* **2015**, *5*, 2305-2313.

(8) Park, E.; Kim, M.; Jung, H.; Chin, S.; Jurng, J. Effect of Sulfur on Mn/Ti Catalysts Prepared Using Chemical Vapor Condensation (CVC) for Low-Temperature NO Reduction. *ACS Catal.* **2013**, *3*, 1518-1525.

(9) Liu, F.; Shan, W.; Lian, Z.; Xie, L.; Yang, W.; He, H. Novel $MnWO_x$ Catalyst with Remarkable Performance for Low Temperature NH_3-SCR of NO_x. *Catal. Sci. Technol.* **2013**, *3*, 2699-2707.

(10) Chang, H.; Chen, X.; Li, J.; Ma, L.; Wang, C.; Liu, C.; Schwank, J. W.; Hao, J. Improvement of Activity and SO_2 Tolerance of Sn-Modified MnOx–CeO_2 Catalysts for NH_3-SCR at Low Temperatures. *Environ. Sci. Technol.* **2013**, *47*, 5294-5301.

(11) Thirupathi, B.; Smirniotis, P. G. Nickel-Doped Mn/TiO_2 as an Efficient Catalyst for the Low-Temperature SCR of NO with NH_3: Catalytic Evaluation and Characterizations. *J. Catal.* **2012**, *288*, 74-83.

(12) Tian, W.; Yang, H.; Fan, X.; Zhang, X. Catalytic Reduction of NO_x with NH_3 over Different-Shaped MnO_2 at Low Temperature. *J. Hazard. Mater.* **2011**, *188*, 105-109.

(13) Jin, R.; Liu, Y.; Wu, Z.; Wang, H.; Gu, T. Low-Temperature Selective Catalytic Reduction of NO with NH_3 over MnCe Oxides Supported on TiO_2 and Al_2O_3: A Comparative Study. *Chemosphere* **2010**, *78*, 1160-1166.

(14) Tao, G.; Helmer, F.; Poul, N. Structural and Morphological Evolution of β-MnO_2 Nanorods during Hydrothermal Synthesis. *Nanotechnology* **2009**, *20*, 055610.

(15) Casapu, M.; Kröcher, O.; Elsener, M. Screening of Doped MnO_x–CeO_2 Catalysts for Low-Temperature NO-SCR. *Appl. Catal. B* **2009**, *88*, 413-419.

(16) Wu, Z.; Jin, R.; Liu, Y.; Wang, H. Ceria Modified MnO_x/TiO_2 as a Superior Catalyst for NO Reduction with NH_3 at Low-Temperature. *Catal. Commun.* **2008**, *9*, 2217-2220.

(17) Kang, M.; Park, E. D.; Kim, J. M.; Yie, J. E. Manganese Oxide Catalysts for NO_x Reduction with NH_3 at Low Temperatures. *Appl. Catal. A* **2007**, *327*, 261-269.

(18) Qi, G.; Yang, R. T.; Chang, R. MnO_x-CeO_2 Mixed Oxides Prepared by Co-Precipitation for Selective Catalytic Reduction of NO

with NH_3 at Low Temperatures. *Appl. Catal. B* **2004**, *51*, 93-106.

(19) Zhan, S.; Zhu, D.; Qiu, M.; Yu, H.; Li, Y. Highly Efficient Removal of NO with Ordered Mesoporous Manganese Oxide at Low Temperature. *RSC Adv.* **2015**, *5*, 29353-29361.

(20) Zhan, S.; Qiu, M.; Yang, S.; Zhu, D.; Yu, H.; Li, Y. Facile Preparation of MnO_2 Doped Fe_2O_3 Hollow Nanofibers for Low Temperature SCR of NO with NH_3. *J. Mater. Chem. A* **2014**, *2*, 20486-20493.

(21) Smirniotis, P. G.; Peña, D. A.; Uphade, B. S. Low-Temperature Selective Catalytic Reduction (SCR) of NO with NH_3 by Using Mn, Cr, and Cu Oxides Supported on Hombikat TiO_2. *Angew. Chem. Int. Ed*. **2001** *40*, 2479-2482.

(22) Pappas, D. K.; Boningari, T.; Boolchand, P.; Smirniotis, P. G. Novel Manganese Oxide Confined Interweaved Titania Nanotubes for the Low-Temperature Selective Catalytic Reduction (SCR) of NO_x by NH_3. *J. Catal.* **2016**, *334*, 1-13.

(23) Boningari, T.; Ettireddy, P. R.; Somogyvari, A.; Liu, Y.; Vorontsov, A.; McDonald, C. A.; Smirniotis, P. G. Influence of Elevated Surface Texture Hydrated Titania on Ce-Doped Mn/TiO_2 Catalysts for the Low-Temperature SCR of NO_x under Oxygen-Rich Conditions. *J. Catal.* **2015**, *325*, 145-155.

(24) Khodayari, R.; Odenbrand, I. C. U. Regeneration of Commercial SCR Catalysts by Washing and Sulphation: Effect of Sulphate Groups on the Activity. *Appl. Catal. B* **2011**, *33*, 277-291.

(25) Liu, Z.; Li, Y.; Zhu, T.; Su, H.; Zhu, J. Selective Catalytic Reduction of NO_x by NH_3 over Mn-Promoted V_2O_5/TiO_2 Catalyst. *Ind. Eng. Chem. Res.* **2014**, *53*, 12964-12970.

(26) Ettireddy, P. R.; Ettireddy, N.; Boningari, T.; Pardemann, R.; Smirniotis, P. G. Investigation of the Selective Catalytic Reduction of Nitric Oxide with Ammonia over Mn/TiO_2 Catalysts through Transient Isotopic Labeling and *in Situ* FT-IR Studies. *J. Catal.* **2012**, *292*, 53-63.

(27) Song, W.; Liu, J.; Zheng, H.; Ma, S.; Wei, Y.; Duan, A.; Jiang, G.; Zhao, Z.; Hensen, E. J. M. A Mechanistic DFT Study of Low Temperature SCR of NO with NH_3 on $MnCe_{1-x}O_2$ (111). *Catal. Sci. Technol.* **2016**, *6*, 2120-2128.

(28) Qi, G.; Yang, R. T. Characterization and FTIR Studies of MnO_x−CeO_2 Catalyst for Low-Temperature Selective Catalytic Reduction of NO with NH_3. *J. Phys. Chem. B* **2004**, *108*, 15738-15747.

(29) Boubnov, A.; Carvalho, H. W. P.; Doronkin, D. E.; Günter, T.; Gallo, E.; Atkins, A. J.; Jacob, C. R.; Grunwaldt, J.-D. Selective Catalytic Reduction of NO Over Fe-ZSM-5: Mechanistic Insights by Operando HERFD-XANES and Valence-to-Core X-Ray Emission Spectroscopy. *J. Am. Chem. Soc.* **2014**, *136*, 13006-13015.

(30) Liu, X.; Yang, Z.; Zhang, R.; Li, Q.; Li, Y. Density Functional Theory Study of Mechanism of N_2O Decomposition over Cu-ZSM-5 Zeolites. *J. Phys. Chem. C* **2012**, *116*, 20262-20268.

(31) Sklenak, S.; Andrikopoulos, P. C.; Boekfa, B.; Jansang, B.; Nováková, J.; Benco, L.; Bucko, T.; Hafner, J.; Dědeček, J.; Sobalík, Z. N_2O Decomposition over Fe-Zeolites: Structure of the Active Sites and the Origin of the Distinct Reactivity of Fe-Ferrierite, Fe-ZSM-5, and Fe-Beta. A Combined Periodic DFT and Multispectral Study. *J. Catal*. **2010**, *272*, 262-274.

(32) Brüggemann, T. C.; Keil, F. J. Theoretical Investigation of the Mechanism of the Selective Catalytic Reduction of Nitrogen Oxide with Ammonia on Fe-Form Zeolites. *J. Phys. Chem. C* **2011**, *115*, 23854-23870.

(33) Wei, Y.; Sun, Y.; Su, W.; Liu, J. MnO_2 Doped CeO_2 with Tailored 3-D Channels Exhibits Excellent Performance for NH_3-SCR of NO. *RSC Adv.* **2015**, *5*, 26231-26235.

(34) Liang, S.; Teng, F.; Bulgan, G.; Zong, R.; Zhu, Y. Effect of Phase Structure of MnO_2 Nanorod Catalyst on the Activity for CO Oxidation. *J. Phys. Chem. C* **2008**, *112*, 5307-5315.

(35) Ettireddy, P. R.; Ettireddy, N.; Mamedov, S.; Boolchand, P.; Smirniotis, P. G. Surface Characterization Studies of TiO_2 Supported Manganese Oxide Catalysts for Low Temperature SCR of NO with NH_3. *Appl. Catal. B* **2007**, *76*, 123-134.

(36) Gu, T.; Jin, R.; Liu, Y.; Liu, H.; Weng, X.; Wu, Z. Promoting Effect of Calcium Doping on the Performances of $MnOx/TiO_2$ Catalysts for NO Reduction with NH_3 at Low Temperature. *Appl. Catal. B* **2013**, *129*, 30-38.

(37) Meng, D.; Zhan, W.; Guo, Y.; Guo, Y.; Wang, L.; Lu, G. A Highly Effective Catalyst of Sm-MnO_x for the NH_3-SCR of NO_x at Low Temperature: Promotional Role of Sm and Its Catalytic Performance. *ACS Catal*. **2015**, *5*, 5973-5983.

(38) Wei, Y.; Liu, J.; Su, W.; Sun, Y.; Zhao, Y. Controllable Synthesis of Ce-Doped α-MnO_2 for Low-Temperature Selective Catalytic Reduction of NO. *Catal. Sci. Technol.* **2017**, *7*, 1565-1572.

(39) Richter, M.; Trunschke, A.; Bentrup, U.; Brzezinka, K. W.; Schreier, E.; Schneider, M.; Pohl, M. M.; Fricke, R. Selective Catalytic Reduction of Nitric Oxide by Ammonia over Egg-Shell MnO_x/NaY Composite Catalysts. *J. Catal.* **2002**, *206*, 98-113.

(40) Smirniotis, P. G.; Sreekanth, P. M.; Peña, D. A.; Jenkins, R. G. Manganese Oxide Catalysts Supported on TiO_2, Al_2O_3, and SiO_2: A Comparison for Low-Temperature SCR of NO with NH_3. *Ind. Eng. Chem. Res.* **2006**, *45*, 6436-6443.

(41) Tang, X.; Hao, J.; Yi, H.; Li, J. Low-Temperature SCR of NO with NH_3 over AC/C Supported Manganese-Based Monolithic Catalysts. *Cataly. Today* **2007**, *126*, 406-411.

(42) Wang, X.; Zheng, Y.; Xu, Z.; Liu, Y.; Wang, X. Low-Temperature NO Reduction with NH_3 over Mn-CeO_x/CNT Catalysts Prepared by a Liquid-Phase Method. *Catal. Sci. Technol.* **2014**, *4*, 1738-1741.

(43) Su, Y.; Fan, B.; Wang, L.; Liu, Y.; Huang, B.; Fu, M.; Chen, L.; Ye, D. MnO_x Supported on Carbon Nanotubes by Different Methods

for the SCR of NO with NH_3. *Catal. Today* **2013**, *201*, 115-121.

(44) Xie, X.; Zhang, C.; Wu, M.-B.; Tao, Y.; Lv, W.; Yang, Q.-H. Porous MnO_2 for Use in a High Performance Supercapacitor: Replication of a 3D Graphene Network as a Reactive Template. *Chem. Commun.* **2013**, *49*, 11092-11094.

(45) Perdew, J. P.; Burke, K.; Ernzerhof, M. Generalized Gradient Approximation Made Simple. *Phys. Rev. Lett.* **1996**, *77*, 3865-3868.

(46) Tang, Y.; Zhang, H.; Cui, L.; Ouyang, C.; Shi, S.; Tang, W.; Li, H.; Lee, J.-S.; Chen, L. First-Principles Investigation on Redox Properties of Doped M-CeO_2 (M = Mn, Pr, Sn, Zr). *Phys. Rev. B* **2010**, *82*, 125104.

(47) Liu, Z.; Xu, K.; Sun, H.; Yin, S. One-Step Synthesis of Single-Layer MnO_2 Nanosheets with Multi-Role Sodium Dodecyl Sulfate for High-Performance Pseudocapacitors. *Small* **2015**, *11*, 2182-2191.

(48) Omomo, Y.; Sasaki, T.; Wang; Watanabe, M. Redoxable Nanosheet Crystallites of MnO_2 Derived *via* Delamination of a Layered Manganese Oxide. *J. Am. Chem. Soc.* **2003**, *125*, 3568-3575.

(49) Gao, T.; Glerup, M.; Krumeich, F.; Nesper, R.; Fjellvåg, H.; Norby, P. Microstructures and Spectroscopic Properties of Cryptomelane-Type Manganese Dioxide Nanofibers. *J. Phys. Chem. C* **2008**, *112*, 13134-13140.

(50) Julien, C.; Massot, M.; Rangan, S.; Lemal, M.; Guyomard, D. Study of Structural Defects in γ-MnO_2 by Raman Spectroscopy. *J. Raman Spectrosc.* **2002**, *33*, 223-228.

(51) Xie, Y.; Yu, Y.; Gong, X.; Guo, Y.; Guo, Y.; Wang, Y.; Lu, G. Effect of the Crystal Plane Figure on the Catalytic Performance of MnO_2 for the Total Oxidation of Propane. *CrystEngComm* **2015**, *17*, 3005-3014.

(52) Liang, X.; Hart, C.; Pang, Q.; Garsuch, A.; Weiss, T.; Nazar, L. F. A Highly Efficient Polysulfide Mediator for Lithium–Sulfur Batteries. *Nat. Commun.* **2015**, *6*, 5682.

(53) Yeom, Y. H.; Wen, B.; Sachtler, W. M. H.; Weitz, E. NO_x Reduction from Diesel Emissions over a Nontransition Metal Zeolite Catalyst: A Mechanistic Study Using FTIR Spectroscopy. *J. Phys. Chem. B* **2004**, *108*, 5386-5404.

(54) Abecassis-Wolfovich, M.; Jothiramalingam, R.; Landau, M. V.; Herskowitz, M.; Viswanathan, B.; Varadarajan, T. K. Cerium Incorporated Ordered Manganese Oxide OMS-2 Materials: Improved Catalysts for Wet Oxidation of Phenol Compounds. *Appl. Catal. B* **2005**, *59*, 91-98.

(55) Wu, Z; Jiang, B.; Liu, Y.; Wang, H.; Jin, R. DRIFT Study of Manganese/Titania-Based Catalysts for Low-Temperature Selective Catalytic Reduction of NO with NH_3. *Environ. Sci. Technol.* **2007**, *41*, 5812–5817.

(56) Li, J.; Chen, J.; Ke, R.; Luo, C.; Hao, J. Effects of Precursors on the Surface Mn Species and the Activities for NO Reduction over MnO_x/TiO_2 Catalysts. *Catal. Commun.* **2007**, *8*, 1896–1900.

(57) Nicosia, D.; Czekaj, I.; Krocher, O. Chemical Deactivation of $V_2O_5/WO_3–TiO_2$ SCR Catalysts by Additives and Impurities from Fuels, Lubrication Oils and Urea Solution: Part II. Characterization Study of the Effect of Alkali and Alkaline Earth Metals. *Appl. Catal. B* **2008**, *77*, 228–236.

(58) Sun, P.; Guo, R.; Liu, S.; Wang, S.; Pan, W.; Li, M. The Enhanced Performance of MnO_x Catalyst for NH_3-SCR Reaction by the Modification with Eu. *Appl. Catal. A* **2017**, *531*, 129–138.

(59) Ettireddy, P.; Kotrba, A.; Boningari, T.; Smirniotis, P. Low Temperature SCR Catalysts Optimized for Cold-Start and Low-Load Engine Exhaust Conditions. *SAE Tech. Pap.* **2015**, 2015-01-1026.

TOC Figure

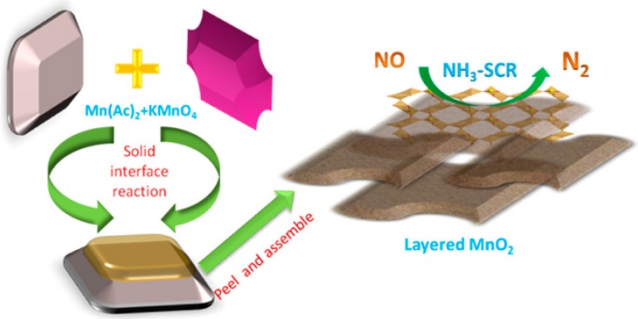
Mn(Ac)2+KMnO4
Solid
interface
reaction
Peel and assemble
NO
NH3-SCR
N2
Layered MnO2